Electrochemical Materials and Technologies

ARTICLE

Electrochemical Materials and Technologies

eISSN: 2949-0561

Cite this: Electrochem. Mater. Technol. 2 (2023) 20232017

Modeling the UO_2 reduction process

Alexander Galashev [a]*, Ksenia Abramova [a], Alexey Vorob'ev [a], Oksana Rakhmanova [a], Yuri Zaikov [a]

Received: 13 July 2023
Accepted: 1 September 2023
Published online: 12 September 2023

DOI: 10.15826/elmattech.2023.2.017

Methods of molecular dynamics and DFT calculations have been used to study the reduction mechanisms of UO_2 as the most representative part of spent nuclear fuel to metallic uranium. It is shown that the critical softening of the combined modulus of elasticity G_{11}-G_{12} to zero is the reason for the destruction of the UO_2 crystal as a result of the removal of oxygen from it. This destruction is accompanied by an order-disorder phase transition in the oxygen subsystem of the crystal under consideration. DFT calculations indicate a continuous decrease in the band gap as oxygen is removed from the UO_2 crystal. When the system reaches the composition U_2O_3, the band gap disappears and the system becomes electrically conductive. The appearance of the dielectric-conductor transition explains the realization of the FFC Cambridge process during the recovery of spent nuclear fuel. The passage of Li^+ and Cl^- ions of the LiCl melt through cylindrical channels in a UO_2 crystal with cross-sectional radii from 0.25 up to 2 nm has been studied. The strength of the external electric field required for the passage of these channels decreases with an increase in the channel cross section, and the number of Cl^- ions entering the channel increases. On the walls of the channels that pass ions with charges of both signs, colonies of adsorbed Cl^- and Li^+ atoms appear separated from each other, between which strong electric fields are formed. The existence of such fields can cause Li^+ ions to move deep into the material being reduced.

keywords: electrical conductivity, electric field, molecular dynamics, nanopore, oxygen, uranium oxides

© 2023, the Authors. This article is published in open access under the terms and conditions of the Creative Commons Attribution (CC BY) license http://creativecommons.org/licenses/by/4.0/).

1. Introduction

Nuclear energy can be seen as a global source of energy that can meet the growing demand for energy and does not release greenhouse gases into the environment. A serious obstacle to the use of nuclear energy is the accumulation of spent nuclear fuel (SNF). At present, the problem of SNF reprocessing is acute. The processing of SNF from light water reactors and the production of metallic fuel, which will be irradiated in a fast neutron nuclear reactor, can be performed using pyroprocessing. This article discusses the process of electrochemical reduction, which is the first step in the electrochemical processing of fuel. High temperature molten salt reprocessing technology has several advantages over aqueous reprocessing techniques. These advantages include reduced material leakage, equipment compactness, a shorter cooling period for irradiated fuel, and also higher safety margins. After unpacking, grinding and granulation, the spent nuclear fuel enters the reactor for electrolytic reduction. During this process, UO_2 is reduced to uranium metal. The recovered product is then subjected to electrorefining [1]. Electrorefining allows you to separate U and transuranium components, which are processed into new fuel. The opinion was established that the electrolytic reduction of SNF includes two main reaction pathways [2]. These are direct electrochemical reduction (1) and reduction occurring at a slightly higher electrode potential through the deposition of lithium metal (2) and (3).

$$UO_2 + 4e^- \rightarrow U\,(\text{cathode}) \quad (1)$$

$$2Li_2O + 4e^- \rightarrow 4Li + O^{2-}(\text{cathode}) \quad (2)$$

$$4Li + UO_2 \rightarrow U + 2Li_2O\,(\text{cathode}) \quad (3)$$

a: Institute of High-Temperature Electrochemistry, Ural Branch of Russian Academy of Sciences, Yekaterinburg 620990, Russia

* Corresponding author: alexander-galashev@yandex.ru

The potential difference between reactions (1) and (2) is only 70 mV. Therefore, it is very difficult to maintain exclusively direct electroreduction. Lithium is also recovered from the electrolyte and participates in the reduction of UO_2.

An experimental study [3] confirmed the correctness of thermodynamic calculations [4], according to which alkali and alkaline earth metals, such as Cs, Ba, and Sr, should diffuse from the fuel and accumulate in the salt phase. Actinide and noble metal oxides are completely reduced by electrolysis, while zirconium oxide undergoes only partial deoxidation. Rare-earth fission products also fail to be converted into metallic forms. In the electrorefining step, unreduced rare earth oxides tend to chemically react with UCl_3. As a result, finely dispersed uranium oxide contaminating the electrorefined salt is formed [5]. Therefore, solving the problem of the rare-earth elements oxides reduction is an important task. The rate of electrochemical reduction is determined by the intensity of diffusion of O^{2-} ions from the oxide fuel into the bulk molten salt. Understanding the mechanisms of the SNF recovery process is one of the main factors that makes it possible to increase the speed of this process, reduce energy costs, and increase the productivity of the cell. A number of details of the SNF electrolytic reduction process, including both experimental and theoretical studies, are described in [6–8]. Special experimental studies on the reduction of zirconium oxide by the electrolytic method showed the possibility of only its partial deoxidation, regardless of the electrolyte used [9, 10].

In [11] a Hubbard corrected density functional theory (DFT+U) study of the properties of hypostoichiometric phases of uranium dioxide was carried out. The transition from a semiconductor to a conductor was shown with an increase in the number of oxygen vacancies in uranium dioxide. In addition, electronic conductivity also appears when UO_2 is heated.

The purpose of this work is to determine the change in the physical characteristics and structure of the hypostoichiometric compound UO_{2-x} as oxygen is removed from this system, and also to understand the mechanism of lithium penetration into the nanoporous structure of the recovered SNF, using the DFT calculations, as well as classical molecular dynamics modeling.

2. Computer models

To solve this problem, in this work, quantum mechanical calculations (DFT calculations) are carried out, as well as classical molecular dynamics modeling of the electrolytic reduction of UO_2.

2.1. *Ab initio* calculations

Calculations were performed using the Siesta software package [12]. The uranium dioxide cell was obtained by combining a 2 x 2 x 2 uranium FCC supercell (8 uranium atoms) and two cubic oxygen lattices (16 oxygen atoms). To simulate the reduction of uranium dioxide vacancies, 1–6 oxygen atoms were removed from the system. For each of the defect systems presented, two initial positions of vacancy defects were considered. The introduction of plutonium is represented by the replacement of one or two uranium atoms by plutonium atoms. The ratio of plutonium to uranium 1 to 7 and 1 to 3 was considered. In systems containing plutonium, only removal of 2 and 4 oxygen atoms was carried out. The simulation was carried out using the LDA + U approximation [13], the values of the parameters U_{eff} and J_{eff} for both uranium and plutonium atoms were taken to be 4.5 and 0.5 eV, respectively. Similar parameters for plutonium atoms were determined as 10 and 0 eV, respectively. Geometric optimization was done using the local density approximation in the CA form [14]. The dynamic relaxation of the positions of atoms and translation vectors continued until the change in the total energy of the system became less than 0.001 eV. The density of the three-dimensional grid used to calculate the electron density was set using a cutoff energy of 550 Ry. The band structure was calculated in the L-Γ-X-U-K-Γ direction. The Brillouin zone was set by the Monkhorst-Pack method [15] using 5 × 5 × 5 k-points.

2.2. Classical molecular dynamics calculations

At the first stage of molecular dynamic simulation (MD), we studied the mechanical stability of the hypostoichiometric UO_{2-x} phases. Figure 1a shows the defect-free UO_2 crystal with fluorite structure, the crystal contained 12000 atoms of both types, MD cell had the following dimensions 5.3 × 5.3 × 5.3 nm. The study was carried out using the periodic boundary conditions. A total of eight systems were considered. The oxygen concentration in each system corresponded to the parameter x, which varied from 0 to 2 with a step of 0.25 (i.e., for each new system, the oxygen concentration decreased by 12.5 %). The distribution of oxygen at the ration N_O/N_U = 2, 1, 0.25 on the (111) surface is shown in Figure 1 (b–d).

The charge-optimized many-particle potential COMB3 [16], which is a modification of the Tersoff potential [17] with the possibility of dynamic charge balancing, was chosen to describe the interaction both in a defect-free UO_2 crystal and in hypostoichiometric

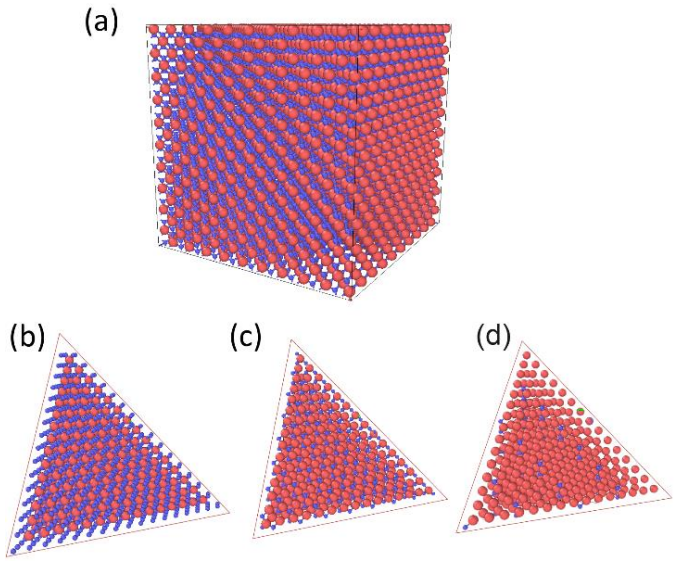

Figure 1 Initial configuration of the simulated system: a) full-scale system of stoichiometric UO_2 containing 12000 atoms of both types; (b)–(d) Images of a cut along the crystallographic plane (111) in hypothetical UO_{2-x} compounds with various inclusions of oxygen in the system: (b) UO_2, (c) UO, (d) $UO_{0.25}$. Uranium atoms are marked in red-brown; oxygen atoms are marked in blue.

UO_{2-x} compounds. When using the COMB3 potential, the total energy can be represented as:

$$U^{tot}(q, r) = U^{es}(q, r) + U^{short}(q, r) + U^{vdW}(q, r) + \\ + U^{corr}(q, r), \quad (4)$$

where U^{es} is the ionization energy of atom; U^{short} is the short-range energy of pairwise interaction; U^{vdW} is the energy due to the presence of van der Waals forces; U^{corr} is the corrections term due to the complex angular interaction.

Thereby, the generalized form of the potential, as well as dynamic charge balancing, makes it possible to use the potential to describe a wide class of compounds, including UO_{2-x} at various oxygen concentrations [18].

Based on the ration N_O/N_U at the initial stage, fractional charges were determined for the particles of the every UO_{2-x} system. In other words, in each case, the charge value was chosen from the condition of general electrical neutrality of the system and the amount of oxygen it contains. Then, using the extended Lagrange method, charges were dynamically balanced by minimizing the electrostatic energy [19]. On the next step, a geometrical optimization procedure by the Polack-Ribière conjugate gradient method was carried out [20]. After the potential energy minimum was found, the system was relaxed in the NPT ensemble at 300 K for 200 ps, reaching equilibrium. Then we proceeded to calculate the elastic moduli of the UO_{2-x} system.

The simulation of the movement of particles of the Li^+, Cl^- melt through the nanopores present in the UO_2 crystal was performed with another form of the interatomic potential. In this case of classical molecular dynamics modeling, the Basak potential [21] was chosen to describe the interaction between uranium and oxygen atoms, in which the Coulomb interaction is represented by fractional charges smaller in magnitude than the valence of the corresponding elements. This potential is written as

$$\varphi_{ij}(r_{ij}) = \frac{z_i z_j e^2}{r_{ij}} + f_0(b_i + b_j)e^{\left(\frac{(a_i + a_j - r_{ij})}{b_i + b_j}\right)} - \\ - \frac{c_i c_j}{r_{ij}^6} + f_0 D_{ij}(e^{-2\beta_{ij}(r_{ij} - r_{ij}^*)} - 2e^{\beta_{ij}(r_{ij} - r_{ij}^*)}), \quad (5)$$

where z_i, z_j are the charge numbers of atoms, e is the elementary charge, a, b, c, f_0, β, r^* are the empirical parameters of the potential presented in Table 1.

The Basak potential (formula 5) contains four terms: 1) the Coulomb term, 2) the contribution representing the repulsion of atomic nuclei, 3) the van der Waals attraction of atoms, and 4) the term describing cross interactions.

Table 1 – Parameters used in the Basak potential.

Parameter	O–O	U–U	U–O
a (Å)	3.82	3.26	3.54
b (Å)	0.327022	0.327022	0.327022
c (· 10^{-19}] Å)	381	0	0
D ($Å^{-1}$)	0	0	13.6765
β ($Å^{-1}$)	–	–	1.65
r^* (Å)	–	–	2.369
f_0	–	–	4.07196

Table 2 – Parameters used in the Tosi-Fumi potential.

Parameter	Li–Li	Li–Cl	Cl–Cl
B(eV)	0.4225	0.29046875	0.1584375
σ (Å)	1.632	2.401	3.170
C(eV $Å^6$)	0.045625	1.25	69.375
D(eV $Å^8$)	0.01875	1.50	139.375

Table 3 – Parameters used in the FIT-LDA potential.

Parameter	Cl–O	Cl–U	Li–O	Li–U
A (eV)	0	5257.4334	486.3405	1655.3252
b ($Å^{-1}$)	1	3.4127322	3.7420981	4.2281046
D(eV)	1.2705	0.0047407	0.0026536	0.0040175
β ($Å^{-1}$)	1.4498	0.3376944	0.4829067	0.1883959
r^*_{ij} (Å)	2.0816	9.9664634	9.2630516	6.4111762

When considering interactions U–U and O–O, this fourth term is assumed to be equal to zero. Uranium and oxygen ions have charges 2.4 a.u. and –1.2 a.u., respectively, *i.e.* U and O atoms are represented as partially ionized.

The Tosi-Fumi potential [22] was used to present interactions of lithium and chlorine atoms:

$$\varphi = Ae^{B(\sigma - r_{ij})} - \frac{C}{r_{ij}^6} - \frac{D}{r_{ij}^8}. \quad (6)$$

The parameters of the Tosi-Fumi potential are given in Table 2.

The potential used to represent Cl–O, Cl–U, Li–O and Li–U interactions was created based on calculations by the electron density functional method (FIT-LDA potentials) [23, 24]

$$\varphi(r_{ij}) = Ae^{-br_{ij}} + D_{ij}(e^{-2\beta_{ij}\left(r_{ij} - r_{ij}^*\right)} - -2e^{\beta_{ij}(r_{ij} - r_{ij}^*)}). \quad (7)$$

The parameters of this potential used for modeling are presented in Table 3. The first step of the simulation was the geometry optimization procedure to find the minimum potential energy of the formed system. Then, after the system was heated to 923 K, it was relaxed under the conditions of the NPT ensemble for 2 ns.

A schematic diagram of modeling the passage of a nanopore by a molten salt in a UO_2 crystal is shown in Figure 2. Here, the molecular dynamics cell was divided into three zones. Initially, zone 1 contained only LiCl molten salt. A UO_2 crystal with a nanopore was located in zone 2. In order to be able to observe the passage of channels with very small cross sections by ions, it was assumed that all atoms of the UO_2 crystal were restricted in movement during the entire calculation time. We will refer to this part of the MD cell as a "semi-mobile" crystal. A cylinder served as the geometric shape of the nanopore; a cylindrical channel connected zones 1 and 3 with each other. An extended UO_2 crystal, the specific volume of which was 2 times bigger than that at 923 K, filled zone 3 and served as a receiver for the ions (Li^+ and Cl^-). When the fission gases Kr and Xe are released, the oxide fuel in a nuclear reactor swells. Light water reactors can also use hydride fuel, the uranium density of which is only 40 % that of oxide fuel [25]. Artificially reducing the density of the extended crystal by 50 % could help to understand the mechanisms of the Li^+ and Cl^- ions diffusion inside the UO_2 crystal during available simulation time (~ 0.1 ns). In some calculations, amorphous UO_2 was used instead of an extended crystal. Changing the structure of the receiver had almost no effect on the simulation result. During the entire simulation time at 923 K, the crystal structure of the ion

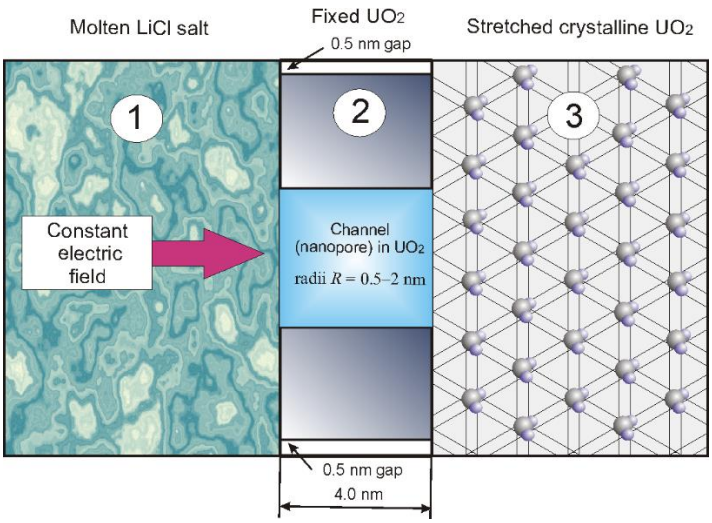

Figure 2 Scheme for modeling the movement of an electrolyte through a cylindrical pore. The numbers indicate the zones of the model cell.

receiver was preserved.

Each cylindrical pore in the UO_2 crystal was built in such a way that the 2 : 1 ratio between oxygen and uranium atoms remained unchanged. U and O atoms located in zone 2 interacted with all atoms and ions in the system. The velocities calculated for them were not reset and corresponded to a temperature of 923 K. However, the movement of atoms was limited to spheres of small radius drawn around the centers of atoms, respectively. The radius of the confining sphere of all these atoms was 0.25 Å. This value is approximately 10 % of the average U–O bond length in the grain uranium dioxide fuel, obtained using X-ray absorption spectroscopy [26]. Due to the specular reflection of atoms from the walls of the confining spheres, the crystal with a pore (channel) did not have significant distortions caused by thermal fluctuations. This guaranteed the preservation of the shape and size of the channel during the entire period of observation of the system.

In order to trace the adsorption of Li^+ and Cl^- ions on the rear face of the "semi-mobile" UO_2 crystal, a ~ 0.5 nm gap was left above and below the "semi-mobile" crystal and the corresponding walls of the MD cell. The gaps were also necessary to prevent the accumulation of identically charged ions not bound to the surface of the UO_2 crystal in zone 1. The presence of these gaps allowed Li^+ and Cl^- ions enter zone 3 through the upper and lower slots, bypassing the cylindrical channel. An external electric field acted between the front wall of the MD cell and the rear surface of the "semi-mobile" crystal, allowing Li^+ and Cl^- ions to pass through the channel and through the flat slots. Supported by an external electric field and smaller in size, Li^+ ions can move to zone 2 and then to zone 3 faster than Cl^- ions. As a result, an excess

of Cl^- ions can be formed in zone 1. Intense interaction between these ions could lead to overheating of the system. Therefore, the presence of gaps in the system is also necessary to maintain its temperature.

Cylindrical channels were considered in the range of radii from 0.25 to 2.0 nm. It was experimentally shown that in order to make the Li^+ and Cl^- ions move along the channel, it is necessary to create an electric field strength E_{ext} in the range from 10^3 to 10^8 V/m. Obviously, for the ion to pass through a narrower channel, it is required to apply an electric field with a higher intensity. A similar problem was solved by the method of controlled molecular dynamics, when the passage of the Ca^{2+} ion through the narrowing section of the pore was studied in [27]. Zone 1 initially contained 2000 Li^+ and Cl^- ions. Zone 2 was constructed from 6000 "semi-mobile" U and O particles. All atoms filling zone 3 were mobile, and their number was 9000. The equations of motion were integrated with a time step $\Delta t = 10^{-16}$ s. The duration of computer calculations varied for channels of different cross sections and ranged from 1 to 2 million time steps. As a rule, the ions passed through the channels over 0.1-0.2 million time steps.

The MD cell used was expanded in the *Oy* and *Oz* directions by periodic boundary conditions, while free boundary conditions were applied in the *Ox* direction to allow the ions to move along the channel.

The generalized Hook's law is written as

$$\sigma_{ij} = C_{ijkl}\varepsilon_{kl}, \quad (8)$$

where σ_{ij} is the stresses arising in the system deformed by the ε_{kl} value. C_{ijkl} is the proportionality coefficient between the given values.

The generic requirements for elastic stability of crystal lattices in the case of cubic crystals reduce to a very simple form [28]:

$$C_{11} - C_{12} > 0,\ C_{11} + 2C_{12} > 0,\ C_{44} > 0. \quad (9)$$

From the condition that all diagonal elements of the elasticity matrix are positive, it follows that $C_{ij} > 0$. Then the second condition in expression (9) is replaced by

$$C_{11} > 0. \quad (10)$$

Second-order elastic constants are defined according to the expression:

$$C_{ij} = \frac{1}{V_0}\left(\frac{\partial^2 E}{\partial\varepsilon_i \partial\varepsilon_j}\right), \quad (11)$$

where E is the energy of the crystal, V_0 its equilibrium volume and ε denotes a strain.

The stress tensor components were calculated by stretching the MD cell by 0.0001 L (where L is the MD cell edge length) under the conditions of the microcanonical (NVE) ensemble.

3. Results

In the ideal lattice of a UO_2 crystal, the U atoms occupy positions corresponding to the sites of the FCC lattice, and the O atoms are located at the centers of the tetrahedral cavities. In other words, an ideal UO_2 crystal has the ideal fluorite structure. However, at the temperature of 923 K, at which the simulation was performed, the O atoms perform significant thermal vibrations and deviate from the initially occupied centers of equilibrium. Sequential removal of oxygen atoms from the system leads to an increase in the free volume that these atoms can occupy. The distributions of the locations of oxygen atoms relative to the centers of the tetrahedral voids of UO_{2-x} crystals, obtained by removing randomly selected O atoms from the system, are shown in Figure 3.

With a decrease in the oxygen concentration up to the preparation of the UO compound, the distributions of the locations of the O atoms relative to the centers of the voids are approximately described by a normal distribution with an average $\mu = 0$. In other words, the oxygen atoms remain in their tetrahedral cavities, oscillating oscillating around the corresponding centers.

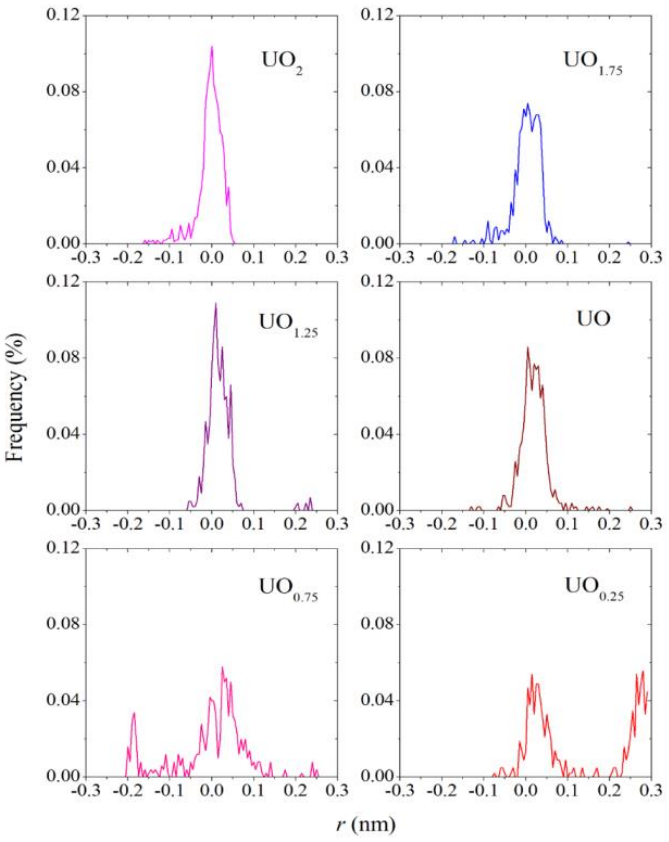

Figure 3 Distribution of oxygen atoms relative to void centers determined by the U-sublattice in UO_{2-x} systems.

However, after the next portion of oxygen extraction, *i.e.* going to the $UO_{0.75}$ compound, the shape of the considered distribution changes significantly: it acquires a jagged shape and spreads out in both directions. This type of distribution under consideration can be explained by the significant displacements of O atoms in the corresponding hypostoichiometric compound, including jumps from one tetrahedral void to another. It is obvious that a structural order-disorder phase transition occurs in the oxygen subsystem. At an even lower oxygen concentration in the system, i.e., for the $UO_{0.25}$ compound, jumps of O atoms between adjacent voids become even more pronounced, and two distinct peaks appear in the corresponding distribution. We emphasize that the structural transition in the oxygen subsystem does not occur gradually, but only after more than half of the O atoms are removed from the compound.

Significant removal of oxygen from the U–O compound ultimately leads to the expected structural rearrangement in the system. The ongoing phase transition can be traced by the change in the elastic moduli of the crystalline system. Figure 4 shows the change in the elastic moduli of the considered crystal as oxygen is removed from this compound. As can be seen from the figure, the most dramatic decrease in the C_{ij} modules occurs when the first quarter of O atoms is removed from the system, *i.e.* until a $UO_{1.5}$ compound is received. With further oxygen depletion, there is a slower decline in C_{ij} values. However, it can be seen that single moduli C_{ij} do not vanish even at very large oxygen removal, *i.e.* before obtaining the composition $UO_{0.25}$.

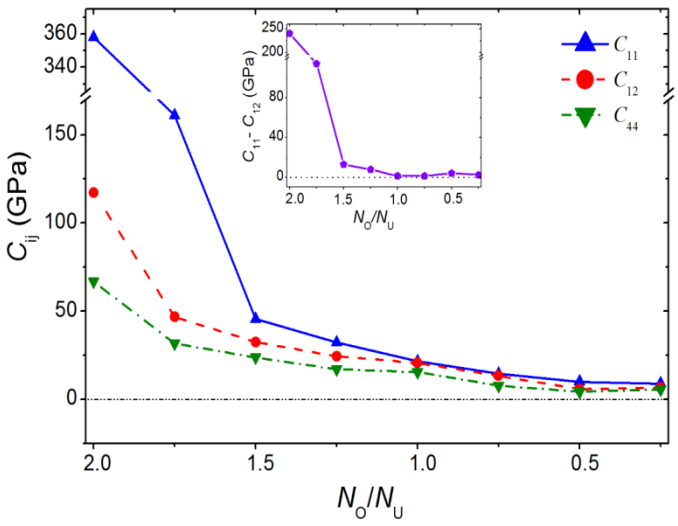

Figure 4 Dependence of the elastic moduli C_{11}, C_{12}, C_{44} (in GPa) on the oxygen content in the UO_{2-x} compound. The inset shows the behavior of the stability criterion $C_{11} - C_{12}$, as a function of the oxygen content.

At the same time, full softening to zero is observed for the module $[C_{11} - C_{12}] = 0$ (see the inset in Figure 4) already upon receipt of the UO connection. Consequently, the instability of the crystal under consideration, which occurs for the composition UO ($[C_{11} - C_{12}] = 0$), is caused by a combination of longitudinal and transverse deformations caused by forces acting in the (100) direction and the direction perpendicular to it. Figure 5 shows the band structure and partial spectrum of electronic states obtained for uranium dioxide. The band gap of UO_2 has a width of 2.23 eV, which is slightly larger than the value of 2.19 eV obtained in [29]. The band gap for PuO_2 calculated by us is also characterized by a lower value (2.49 eV) than the similar value (2.64 eV) determined in [30]. Figure 6 shows the dependence of the band gap as a function of the amount of oxygen in the system. From the figure it can be seen that the conduction in defected uranium dioxide occurs when 4–6 oxygen atoms are removed, *i.e.* when the ratio of oxygen to uranium in the system is in the range from 1.5 to 1.25. The difference in the composition of the system at which the conducting state is reached is due to the different sequence of removal of oxygen atoms from the system. The conductive properties in hypothetical U_8O_{12} and U_8O_{10} compounds appear due to the interaction of the *d* and *f* orbitals of uranium with the p orbitals of oxygen. The narrowing of the band gap and the transition to a conducting phase in hypostoichiometric uranium compounds are consistent with the data obtained in [11].

Table 4 shows the band gap for the considered oxides and average Mulliken charges calculated for uranium, plutonium, and oxygen atoms. The replacement of uranium by plutonium in a ratio of 7 to 1 leads to a narrowing of the band gap of the studied oxide from 2.23 to 1.11 eV. With further removal of oxygen from the system, a semiconductor-conductor transition is achieved. Here, there is a certain analogy with the mixing of CuO and TiO_2 oxides [31]. Synthesis of heterostructures based on mixing a narrow-gap semiconductor in the form of CuO oxide with TiO_2 having a band gap of 3.2 eV produces an exceptionally narrow band-gap semiconductor that is used for visible light-driven photocatalysis. Replacing uranium with plutonium in the UO_2 compound until U/Pu = 3 : 1 leads to metallization of uranium dioxide due to a shift of the Fermi level. However, when removing from the resulting compound of two oxygen atoms, a transition to a semiconductor state with a band gap of 0.72 eV is achieved. With the further removal of oxygen from the system, a conductive state is re-formed. The narrowing of the band gap is caused by the difference in the

electron shells between the uranium and plutonium atoms. Table 4 shows that plutonium atoms in compounds have from 42 to 106 % higher elementary charge compared to uranium atoms. Thus, the following pattern can be traced at the considered compositions of the actinide mixed oxide: if the average charge of plutonium is higher than the charge of uranium by more than 50 %, then the compound becomes a conductor, if less, then a mixed oxide has semiconductor properties.

Figure 7 shows the partial density of the electronic states for the U_7PuO_{16}, U_7PuO_{14}, $U_6Pu_2O_{16}$ and $U_6Pu_2O_{14}$ systems. Conductivity appears in the U_7PuO_{14} and $U_6Pu_2O_{16}$ compounds due to the interaction of 5*f* uranium and plutonium orbitals with 2*p* oxygen orbitals.

Table 4 – The band gap of the oxides and the average Mulliken charges for uranium, plutonium, and oxygen atoms.

N_{Pu}	N_O	Band gap, eV	Q_U, a.u.	Q_{Pu}, a.u.	Q_O, a.u.
0	16	2.23	1.62	–	–0.81
	14	0.99	1.52	–	–0.76
	12	metal	1.50	–	–0.75
1	16	1.11	1.39	2.05	–0.74
	14	metal	1.25	1.91	–0.76
	12	metal	1.05	1.72	–0.75
2	16	metal	1.31	2.71	–0.83
	14	0.72	1.41	2.01	–0.81
	12	metal	0.91	1.78	–0.79

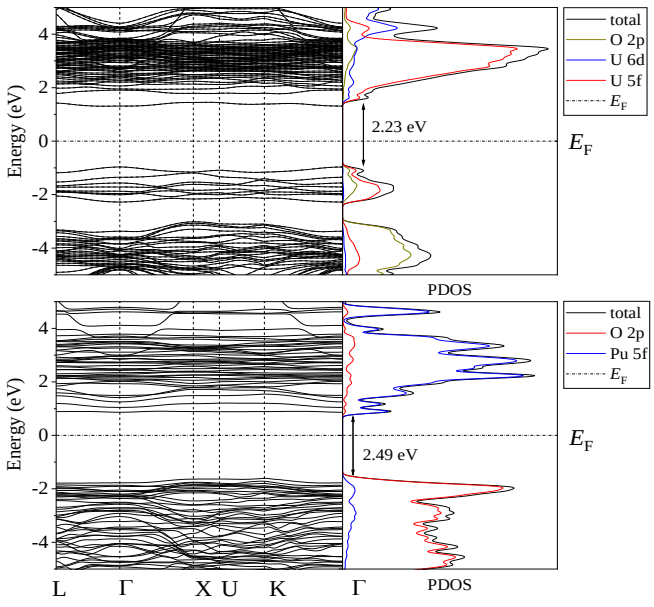

Figure 5 Band structure and spectrum of electronic states of uranium dioxide (top) and plutonium dioxide (bottom); the horizontal dotted line indicates the position of the Fermi energy (E_F), which is set to zero.

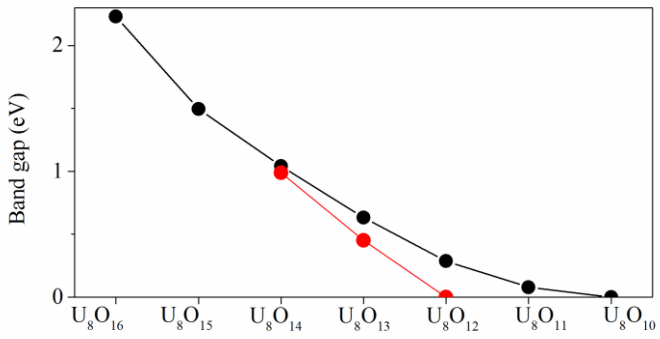

Figure 6 Value of the band gap of hypostoichiometric "phases" of U_yO_x.

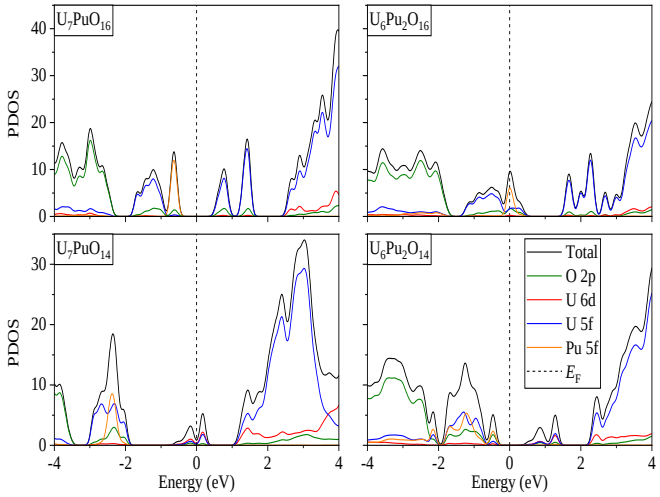

Figure 7 Partial density of electronic states obtained for compounds U_7PuO_{16}, U_7PuO_{14}, $U_6Pu_2O_{16}$ and $U_6Pu_2O_{14}$.

Separated by type of electric charge (+ and –), electrolyte ions deposited on nanopore walls create an induced electric field E_{ind} in the system, which can be estimated from the relation:

$$E_{ind} = \frac{4Q_{Cl}}{RL}, \qquad (12)$$

where $Q_{Cl} = \sum_{i=1}^{N_{Cl}} q_{Cl}$ is the total charge of all chloride ions in the nanopore, taking into account the fact that the number of Cl^- ions in the channel is always less than the number of Li^+ ions; L is the average length of a Cl^- ion colony along the channel axis.

The narrowest of the considered channels (R = 0.25 nm) was filled exclusively with lithium ions when an electric field of 10^8 V/m was applied. At lower electric fields, Li^+ ions got stuck in the channel. The configuration of the system with a nanopore with a cross section radius of 0.25 nm, when exposed to an electric field with strength of 10^8 V/m at the time instant of 0.01 ns, is shown in Figure 8.

Under the action of the external electric field (E_{ext}) directed along the Ox axis, the Li^+ electrolyte ions move

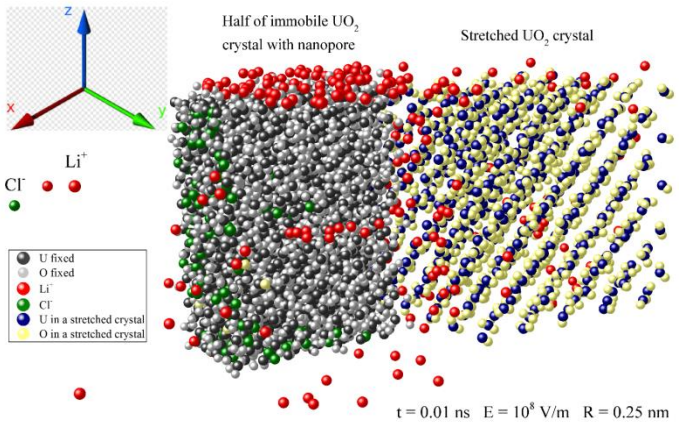

Figure 8 System configuration "LiCl + crystal UO_2 (containing a nanopore) + stretched UO_2 crystal" at time to $t = 0.01$ ns, with a channel radius of 0.25 nm and an applied external field of $E_{ext} = 10^8$ V/m. "Semi-mobile" UO_2 is represented by the central longitudinal section.

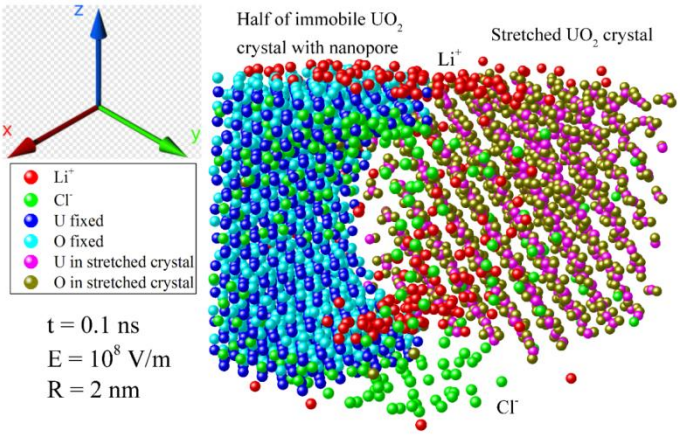

Figure 9 System configuration "LiCl + crystal UO_2 (containing a nanopore) + stretched UO_2 crystal" at time of $t = 0.1$ ns, with a channel radius of 2.0 nm and an applied external field of $E_{ext} = 10^8$ V/m. "Semi-mobile" UO_2 is represented by the central longitudinal section.

Table 5 – The estimated values of the induced electric field strength E_{ind} in the nanopores of radii $R = 0.5–2$ nm in UO_2 crystal at different values of the applied external electric field. [a]

Radius of nanopore, nm	Applied external electric field strength E_{ext}, V/m		
	10^6	10^7	10^8
0.5	$3.33 \cdot 10^{11}$ (0.1 ns)	$3.57 \cdot 10^{11}$ (0.1 ns)	$5.41 \cdot 10^{11}$ (0.01 ns)
1.0	$7.5 \cdot 10^{10}$ (0.05 ns)	$11.3 \cdot 10^{10}$ (0.08 ns)	$10.0 \cdot 10^{10}$ (0.04 ns)
1.5	$11.1 \cdot 10^{10}$ (0.1 ns)	$7.6 \cdot 10^{10}$ (0.08 ns)	$7.2 \cdot 10^{10}$ (0.1 ns)
2.0	$5.2 \cdot 10^{10}$ (0.1 ns)	$5.3 \cdot 10^{10}$ (0.06 ns)	$6.03 \cdot 10^{10}$ (0.1 ns)

[a] – Data in round brackets show the total time of ion deposition on the inner wall of the nanopore in ns.

towards the nanopore. It is possible for them to pass not only along the channel (nanopore), but also in the gaps above and below the "semi-mobile" UO_2 structure. During the specified calculation time, the upper wall of UO_2 is covered with lithium ions. Some Li^+ ions fill the channel. In addition, a significant amount of Li^+ ions reach the UO_2 crystal, and incorporated into its stretched lattice.

The determining factors of lithium motion along the channel are the nanopore radius and the magnitude of the applied electric field. For example, at a channel radius of $R = 1$ nm and a field of $E_{ext} = 10^6$ V/m, by the time of $t = 0.05$ ns, the lithium in the channel leaves it, passing into zone 3.

With an increase in the channel radius to $R = 1.5–2.0$ nm, at the initial time moments (during the first few tens of thousands of steps), a noticeable part of lithium ions (about 1/3) enters the channel, partially settles on the channel walls, and remains in it until the end of the calculation (Figure 9). In this case, zone 1 is completely freed from electrolyte ions. In all cases, Cl^- ions are fixed on the frontal face of crystalline UO_2, which is entirely represented by charged U atoms.

An external electric field of 10^3 V/m during the calculation time of 17.9 ps efficiently promotes ions into the channel. In this case, together with lithium ions, Cl^- ions are trapped into the channel in large numbers. They, like Li^+ ions, settle in special places on the channel walls, and also move more slowly (comparing stronger electric fields) towards zone 3.

The estimated values of the induced electric field strength E_{ind} (V/m) in nanopores (with radius $R = 0.5–2$ nm) of the UO_2 crystal at different values of the applied electric field are given in Table 5. The time of observation of ion adsorption for each system is indicated in parentheses. The strongest induced fields are observed for small nanopore ($R = 0.5$ nm). As the radius of the channel (nanopore) increases, the magnitude of the induced electric field, as a rule, decreases.

4. Discussion

The fabrication of SNF pellets for further pyroprocessing into metallic fuel involves a milling process to convert the spent light water reactor (LWR) fuel pellet to powder. This powder contains all of the actinides and most of the fission products from irradiation in the LWR. Before sintering and pressing, the powder can be enriched with natural uranium. It is known that in the samples that have undergone heat treatment, a weakening of the grain boundaries is observed. The stress concentration is the basis for the

formation of microcracks, so microcracks almost always form during hot stamping. Thus, pores and cracks must be present in the pellets loaded into the cathode basket for electrolytic processing. This fact is taken into account in this work in order to establish the mechanism for the movement of Li^+ ions deep into the processed material. Lithium ions entering the SNF granule directly connected to the cathode are converted into lithium atoms and participate in the reaction of converting UO_2 into metallic uranium.

The passage of Li^+ and Cl^- electrolyte ions through the cylindrical pores of various radii (0.25–2 nm) in crystalline α-UO_2 under the action of the external applied electric field $E_{ext} = 10^3$–10^8 V/m is studied. Nanopores of the smallest radius ($R = 0.25$ nm) turn out to be "permeable" only for Li^+ ions and are clogged by these ions over time. On the walls of channels with a larger radius $R = 0.5$–2 nm, Li^+ and Cl^- ions partially settle in the form of colonies of ions with charges of the same sign and do not leave the channel until the end of the simulation time (0.1 ns). As a result of the accumulation of separated charges of the opposite sign, an induced electric field is formed on the nanopore walls. The strength of the induced field, as a rule, decreases with increasing nanopore radius in crystalline UO_2.

The applied external electric fields necessary for the movement of ions through cylindrical channels are comparable with the average value of the electric field ($0.3 \cdot 10^7$ V/m), which causes a plasma discharge that ionizes hydrogen at atmospheric pressure at a distance between electrodes of 400 μk [32]. In this case, the peak value of the electric field was found at the cathode ($1.07 \cdot 10^7$ V/m), where the maximum electron temperature (7.5 eV) and the maximum density of ions and electrons were also observed. At the same time, the electron temperature near the anode was about 2.4 eV. A stable glow discharge was maintained at these parameters.

Understanding the molecular basis of uranium and other actinide recovery from spent nuclear fuel is important for more accurate prediction and appearance of uranium in nuclear waste disposal sites and improving the pyroprocessing process. No rigorous experimental confirmation has been made yet of the possibility of direct reduction of uranium metal in an electrolytic process, although such attempts have been made. In [33], high-density UO_2 pellets were reduced in molten $CaCl_2$–48 mol % NaCl at 923 K in the constant voltage (3.3 V) and constant current modes using graphite as an anode. No Ca-U-O or Na-U-O type ternary intermediates or suboxides were observed at the end of the reduction process. Also, a large consumption of the graphite anode was not recorded, and the contamination of the melt with carbon was minimal. The UO_2 tablets were completely reduced if the electrolysis time exceeded 35 hours. At a shorter electrolysis time, only surface reduction was observed. Due to the presence of small side effects, this experiment cannot be considered as a rigorous proof of passing the direct reduction of uranium metal from UO_2.

Until now, there is no complete clarity on the possibility of passing a single-step process with 4 electrons in the electroreduction of TiO_2 in molten salt (Cambridge FFC process [34]), since the experimental results deviate from theory [35]. In other words, the actual path of electrochemical reduction cannot be considered as strictly established one [36, 37].

We have considered the process of electrolytic reduction of uranium dioxide based on a simple model of the gradual removal of oxygen from the system. It was found that when the composition of UO is reached, the system loses its mechanical stability, i.e. from this moment, the destruction of the crystal structure at 923 K, which is characteristic of UO_2, should begin. In this case, the order-disorder phase transition is clearly observed in the oxygen subsystem, after more than half of the O atoms have left it. Moreover, the removal of such and even a slightly smaller number of oxygen atoms from the system makes it electrically conductive.

In this paper, we show the mechanism by which the Cambridge FFC process can be implemented in the reduction of UO_2 to uranium metal. The essence of this mechanism lies in the fact that as oxygen leaves the cathode basket loaded with SNF, a gradual increase in the electrical conductivity of the contents of the basket occurs. In other words, with the loss of oxygen, uranium oxides become more and more electrically conductive. Eventually, after the band gap disappears, the direct reduction process becomes preferable to chemical reduction using lithium metal. Most likely, in different parts of the system, both recovery processes occur simultaneously with one or another intensity. To prove that the reduction of UO_2 can be achieved solely by the Cambridge FFC process, it is necessary to remove the electrolyte from the system, convert UO_2 to a metallic state by, for example, applying high pressure, and then remove oxygen from the system due to a strong electric field.

DFT studies of materials like UO_2 or PuO_2 are difficult using the traditional local density approximation (LDA) or generalized gradient approximation (GGA) due to the strong Coulomb correlation of actinide 5*f* electrons. In traversing the actinide elements from Th to Pu, filling bonding and

then antibonding states results in a commonly observed parabolic decrease for volume and delocalized (itinerant) 5*f* states [38]. However, when traversing the actinide elements after Pu in the periodic table, the volume increases because 5*f* electrons tend to localize, leaving the $(spd)^3$ electrons, and begins to take the lead in the bonding in the metal. In the intraband Coulomb interaction named DFT+U proposed in [39], the separation of the total variation space into a localized *d*- / *f*-orbital subspace was performed. Coulomb interaction between these subspaces is treated with a Hubbard-type term in the Hamiltonian. In addition, the subspace of all other states is treated with the local density approximation for Coulomb interaction. LDA+U serves better than GGA+U in DFT calculation, regardless of whether the relativistic effect in the form of Spin-orbit coupling [40] is included in the consideration.

The present study showed that the appearance of Pu in the UO_x compound affects the electronic properties of the system in a similar way as the creation of oxygen vacancies in it. In both cases, the electronic structure of the entire system is rearranged in such a way that it leads to the appearance of socialized electrons that are weakly bound to cations of uranium. As a result, electronic conductivity appears in the system. The difference in the process of socialization is that when oxygen vacancies are created, electrons detached from U atoms are socialized due to the appearance dangling bonds, while when uranium is replaced by plutonium, the Pu atom delegates its electron to the conduction band.

Using the LDA+U approximation to represent exchange-correlation interactions is the first step to discovering the behavior of nuclear materials and understanding the fundamental physics of correlated electrons. Research in this direction should provide new insight into the complex nature of correlated electrons.

5. Conclusion

Thus, the UO_{2-x} crystal is able to retain its structure with a large number of infrequently filled oxygen vacancies. The replacement of U atoms by Pu atoms enhances the electrically conductive properties of the system in question. The appearance of plutonium in uranium oxides makes the process of their reduction faster, because in addition to the chemical reduction mechanism caused by the reduction of penetrating lithium ions and the combination of Li atoms with neighboring oxygen atoms, a direct electronic reduction mechanism becomes possible. The (FFC) Cambridge UO_2 direct reduction process is made possible by the acquisition of electronic conductivity after the removal of less than half of the oxygen from the system. The specificity of the crystal structure of UO_2, expressed in the existence of U- and O-crystallographic planes, contributes to the separation of Li^+ and Cl^- ions during their adsorption on the face of the UO_{2-x} crystal and on the surface of nanopores in it. The separation of charges of different signs leads to the creation of strong local electric fields, due to which Li^+ ions can pass deep into the porous material. The preferential movement of Li^+ ions through nanopores is facilitated by the effect of capillary electrophoresis, which occurs due to the high value of the charge-to-radius ratio for this ion.

Supplementary materials

This manuscript contains supplementary materials, which are available on a corresponding online page.

Funding

This work is executed in the frame of the scientific theme of Institute of High-Temperature Electrochemistry UB RAS, number FUME-2022-0005, registration number 122020100205-5.

Acknowledgments

The calculations were performed on a hybrid cluster-type computer "URAN" at the Institute of Mathematics and Mechanics, Ural Branch of the Russian Academy of Sciences.

Author contributions

Alexander Galashev: Conceptualization; Data curation; Formal Analysis; Writing – original draft; Writing – Review & Editing.

Ksenia Abramova: Resources; Software; Validation; Visualization; Writing – original draft.

Alexey Vorob'ev: Resources; Software; Validation; Visualization; Writing – original draft.

Oksana Rakhmanova: Resources; Software; Validation; Visualization; Writing – original draft.

Yuri Zaikov: Funding acquisition; Data curation; Methodology; Project administration; Supervision.

Conflict of interest

The authors declare no conflict of interest.

Additional information

http://watercluster.ucoz.ru/

References

1. Galashev AY, Processing of fast neutron reactor fuel by electrorefining: Thematic overview, Int. J. Energy Res. **45 (8)** (2021) 11459–11478. https://doi.org/10.1002/er.6267

2. Herrmann SD, Li SX, Simpson MF, Phongikaroon S, Electrolytic reduction of spent nuclear oxide fuel as part of an integral process to separate and recover actinides from fission products, Separation Sci. Technol. **41 (10)** (2006) 1965–1983. https://doi.org/10.1080/01496390600745602

3. Choi E-Y, Jeong SM, Electrochemical processing of spent nuclear fuels: An overview of oxide reduction in pyroprocessing technology, Prog. Nat. Sci.: Mater. Intern. **25 (6)** (2015) 572–582. https://doi.org/10.1016/j.pnsc.2015.11.001

4. Herrmann S, Li S, Simpson M, Electrolytic reduction of spent light water reactor fuel bench-scale experiment results, J. Nucl. Sci. Technol. **44 (3)** (2007) 361–367. https://doi.org/10.1080/18811248.2007.9711295

5. Kang YH, Hwang SC, Lee HS, et al., Effects of neodymium oxide on an electrorefining process of uranium, J. Mater. Proc. Technol. **209 (11)** (2009) 5008–5013. https://doi.org/10.1016/j.jmatprotec.2009.01.024

6. Galashev AY, Ivanichkina KA, Zaikov YP, Computational study of physical properties of low oxygen UO_{2-x} compounds, J. Solid State Chem. **286** (2020) 121278. https://doi.org/10.1016/j.jssc.2020.121278

7. Galashev AY, Manzhurov AI, Zaikov YP, Computer modeling of electrochemical processing of waste nuclear fuel, Int. J. Energy Research, **45(8)** (2021) 11664–11676. https://doi.org/10.1002/er.5462

8. Galashev AY, Recovery of actinides and fission products from spent nuclear fuel via electrolytic reduction: Thematic overview, Int. J. Energy Res. **46(4)** (2022) 3891–3905. https://doi.org/10.1002/er.7458

9. Shishkin AV, Shishkin VY, Nikolaev AY, et al., Reduction of ZrO_2 in LiCl-Li_2O melt during electrolysis, J. Electrochem. Soc. **169** (2022) 116506. https://doi.org/10.1149/1945-7111/ac9f73

10. Nikolaev A, Suzdaltsev A, Pavlenko O, et al., Reduction of ZrO_2 during SNF pyrochemical reprocessing, J. Electrochem. Soc. **168** (2021) 036506. https://doi.org/10.1149/1945-7111/abe8be

11. Kaloni TP, Onder N, Pencer J, Torres E, DFT + U approach on the electronic and thermal properties of hypostoichiometric UO_2, Ann. Nucl. Energy, **144** (2020) 107511. https://doi.org/10.1016/j.anucene.2020.107511

12. Soler JM, Artacho E, Gale JD, et al., The SIESTA method for ab initio order-N materials simulation, J. Phys.: Condens. Matter, **14** (2002) 2745. https://doi.org/10.1088/0953-8984/14/11/302

13. Dudarev SL, Botton GA, Savrasov SY, et al., Electron-energy-loss spectra and the structural stability of nickel oxide: An LSDA+U study, Phys. Rev. B, **57** (1998) 1505. https://doi.org/10.1103/PhysRevB.57.1505

14. Perdew JP, Zunger A, Self-interaction correction to density-functional approximations for many-electron systems, Phys. Rev. B, **23** (1981) 5048. https://doi.org/10.1103/PhysRevB.23.5048

15. Monkhorst HJ, Pack JD, Special points for Brillouin-zone integrations, Phys. Rev. B, **13** (1976) 5188. https://doi.org/10.1103/PhysRevB.13.5188

16. Liang T, Shan T-R, Cheng Y-T, et al., Classical atomistic simulations of surfaces and heterogeneous interfaces with the charge-optimized many body (COMB) potentials, Mater. Sci. Eng.: R: Reports, **74 (9)** (2013) 255–79. https://doi.org/10.1016/j.mser.2013.07.001

17. Tersoff J, Modelng solid-state chemistry: Interatomic potentials for multicomponent systems, Phys. Rev. B: Condens. Matter Mater. Phys. **39** (1989) 5566. https://doi.org/10.1103/PhysRevB.39.5566

18. Phillpot SR, Antony AC, Shi L, et al., Optimized many body (COMB) potentials for simulation of nuclear fuel and clad, Comp. Mater. Sci. **148** (2018) 231–241. https://doi.org/10.1016/j.commatsci.2018.02.041

19. Nakano A, Parallel multilevel preconditioned conjugate gradient approach to variable-charge molecular dynamics, Comp. Phys. Commun. **104 (1–3)** (1997) 59–69. https://doi.org/10.1016/S0010-4655(97)00041-6

20. Grippo L, Lucidi S, A global convergent version of the Polak-Ribiere conjugate gradient method, Math. Program. **78** (1997) 375–391. https://doi.org/10.1007/BF02614362

21. Basak CB, Sengupta AK, Kamath HS, Classical molecular dynamics simulation of UO_2 to predict thermophysical properties, J. Alloys and Compounds, **360 (1–2)** (2003) 210–216. https://doi.org/10.1016/S0925-8388(03)00350-5

22. Tosi MP, Fumi FG, Ionic sizes and born repulsive parameters in the NaCl-type alkali halides–II: The generalized Huggins-Mayer form, J. Phys. Chem. Solids, **25 (1)** (1964) 45–52. https://doi.org/10.1016/0022-3697(64)90160-X

23. Nekrasov KA, Galashev AE. Diffusion of oxygen ions during electrochemical reduction of uranium dioxide in LiCl melt. Molecular dynamics modeling, collection of abstracts. In: Abstracts of the VIII scientific seminar "Modeling of nuclear fuel cycle technologies"; 2019.01.28–2019.02.01, Snezhinsk, Russia. p. 18.

24. Oda T, Oya Y, Tanaka S, Weber WJ, Validation of potential models for Li_2O in classical molecular dynamics simulation, J. Nucl. Mater. **367–370** (2007) 263–268. https://doi.org/10.1016/j.jnucmat.2007.03.139

25. Olander DR, Nuclear fuels: Present and future, Engineering J. **13 (1)** (2009) 1–28. https://doi.org/10.4186/ej.2009.13.1.1

26. Mieszczynski C, Kuri G, Bertsch J, et al., Microbeam x-ray absorption spectroscopy study of chromium in large-grain uranium dioxide fuel, J. Phys. Condens. Matter, **26 (35)** (2014) 355009. https://doi.org/10.1088/0953-8984/26/35/355009

27. Mowrey DD, Xu L, Mei Y, et al., Ion-pulling simulations provide insights into the mechanisms of channel opening of the skeletal muscle ryanodine receptor, J. Biol. Chem. **292 (31)** (2017) 12947–12958. https://doi.org/10.1074/jbc.M116.760199

28. Mouhat F, Coudert F-X, Necessary and sufficient elastic stability conditions in various crystal systems, Phys. Rev. B, **90** (2014) 224104. https://doi.org/10.1103/PhysRevB.90.224104

29. Dugan CL, Peterson GG, Mock A, et al., Electrical and material properties of hydrothermally grown single crystal (III)

UO_2, Eur. Phys. J. B, **91** (2018) 67. https://doi.org/10.1140/epjb/e2018-80489-x

30. Prodan ID, Scuseria GE, Martin RL, Assessment of metageneralized gradient approximation and screened Coulomb hybrid density functionals on bulk actinide oxides, Phys. Rev. B. **73** (2006) 045104. https://doi.org/10.1103/PhysRevB.73.045104

31. Hamad H, Elsenety MM, Sadik W, et al., The superior photocatalytic performance and DFT insights of S-scheme CuO@TiO_2 heterojunction composites for simultaneous degradation of organics, Sci. Rep. **12** (2022) 2217. https://doi.org/10.1038/s41598-022-05981-7

32. Farouk T, Farouk B, Staack D, et al., Modeling of direct current micro-plasma discharges in atmospheric pressure hydrogen, Plasma Sources Sci. Technol. **16** (2007) 619–634. https://doi.org/10.1088/0963-0252/16/3/023

33. Sri Maha Vishnu D, Sanil N, Panneerselvam G, et al., Mechanism of direct electrochemical reduction of solid UO_2 to uranium metal in $CaCl_2$-48mol% NaCl melt, J. Electrochem. Soc. **160 (9)** (2013) D394. https://doi.org/10.1149/2.080309jes

34. Chen GZ, Fray DJ, Farthing TW, Direct electrochemical reduction of titanium dioxide to titanium in molten calcium chloride, Nature, **407** (2000) 361–364. https://doi.org/10.1038/35030069

35. Gruber H, Krautz E, Magnetoresistance and conductivity in the binary-system titanium oxygen. II. Semiconductive titanium-oxides, Phys. Status Solidi A, **69** (1982) 287–295. https://doi.org/10.1002/pssa.2210750222

36. Chen GZ, Fray DJ, Voltammetric studies of the oxygen-titanium binary system in molten calcium chloride, J. Electrochem. Soc. **149 (11)** (2002) E455–E467. https://doi.org/10.1149/1.1513985

37. Dring K, Dashwood R, Inman D, Voltammetry of titanium dioxide in molten calcium chloride at 900°C. J. Electrochem. Soc. **152 (3)** (2005) E104–E113. https://doi.org/10.1149/1.1860515

38. Moten SA, Atta-Fynn R, Ray AK, Huda MN, Size effects on the electronic and magnetic properties of PuO_2 (111) surface, J. Nucl. Mater. **468** (2016) 37–45. https://doi.org/10.1016/j.jnucmat.2015.11.009

39. Anisimov VI, Zaanen J, Andersen OK, Band theory and Mott insulators: Hubbard U instead of Stoner I, Phys. Rev. B, **44** (1991) 943. https://doi.org/10.1103/PhysRevB.44.943

40. Wang H, Konashi K, LDA + U study of Pu and PuO_2 on ground state with spin–orbital coupling, J. Alloys Compounds, **533** (2012) 53–57. https://doi.org/10.1016/j.jallcom.2012.03.117